Survey on Integrated Sensing and Communication Performance Modeling and Use Cases Feasibility

Silvio Mandelli*, Marcus Henninger*†, Maximilian Bauhofer†, Thorsten Wild*

*Nokia Bell Labs Stuttgart, 70469 Stuttgart, Germany

†Institute of Telecommunications, University of Stuttgart, 70569 Stuttgart, Germany

silvio.mandelli@nokia-bell-labs.com

Abstract— **As the research community starts to address the key features of 6G cellular standards, one of the agreed bridge topics to be studied already in 5G advanced releases is Integrated Sensing and Communication (ISAC). The first efforts of the research community are focusing on ISAC enablers, fundamental limits, and first demonstrators, that show that the time has come for the deployment of sensing functionalities in cellular standards.**

This survey paper takes a needed step towards ISAC deployment, providing an analytical toolkit to model cellular systems' sensing performance, accounting for both their fundamental and practical constraints. We then elaborate on the likely features of 6G systems to provide the feasible sensing key performance indicators (KPIs) in the frequency ranges spanned by cellular networks, including the potential new bands available in 6G, the Frequency Range 3 (FR3).

We further validate our framework by visually investigating ISAC constraints with simulation examples. Finally, we assess the feasibility of few selected scenarios that can be enabled by ISAC, highlighting in each of them the limiting factor and, thus, which gaps should be filled by the research and standardization communities in the next years.

Index Terms—**Integrated sensing and communication, 6G, performance modeling, use cases feasibility.**

I. INTRODUCTION

The next generations of wireless networks will define the key enablers for the applications and services of the next decade. Focusing on cellular systems, the sixth generation (6G) cellular standard aims at boosting communications performance and flexibility compared to the previous fifth generation (5G) releases [1]. Among the disruptive topics studied by the 6G research community, Integrated Sensing and Communication (ISAC) has been raising interest, given the revolution that it brings in communication systems' hardware, software, and architecture [2], [3]. In particular, the increased carrier bandwidths enabled at higher frequencies together with their aggregation opportunities [4], [5], and the deployment of massive antenna arrays [2], made possible to consider running wireless networks as radars. This is a considerable step from 5G's active localization, where the goal was to locate active users as in [6], that were collaborating in their localization. With 6G ISAC, the wireless network scans and acquires information from a passive environment.

Accordingly, the ISAC topic has already been object of different conferences and workshops, discussing first concepts and demonstrators, or recapping the basics in comprehensive surveys [2], [7] or public projects' deliverables [8]. The authors of this paper have participated in the world's first ISAC demonstrator at mmWave (28 GHz), performing both communications and mono-static sensing [3], showcased at the Mobile World Congress 2023 in Barcelona.

To the best of our knowledge, the existing works on ISAC focus on optimization of its performance and enablers, e.g., on the necessary hardware and architecture design [3]. The existing surveys [2], [7] discuss use cases and relevant key performance indicators (KPIs). On the other hand, the radar literature [9] neglects the constraints and parameterization that is needed when also communications has to be considered. The closest work to ours [7] provides an excellent analytical study on the sensing KPIs, focusing on achievable performance bounds in the presence of noise, and the effect of resolution on performance. However, the authors do not provide considerations on the inter-relationships between the effects that may limit sensing performance in ISAC and do not comment on the performance achievable, according to 6G systems' foreseen features and parameters. Therefore, in this survey we aim at jointly analyzing the relevant effects that determine the sensing KPIs of an ISAC system, focusing on typical radar impairments and the limitations given by communications features. In particular, this paper provides:

- The needed analytical tools to assess the impact of thermal noise, quantization noise, and resolution in a single ISAC system (Section II).
- In Section III, a characterization of feasible ISAC systems' features and parameters for each of the different frequency ranges that are currently being considered for 6G [1] or are already in use for 5G, except the sub-THz spectrum which we expect to initially not play the strongest role in early 6G [3]:
  - Frequency Range 1 (FR1): from 600 MHz to 6 GHz,
  - Frequency Range 2 (FR2): mmWave, 24 GHz to 71 GHz,
  - the new Frequency Range 3 (FR3), that is not yet specified: from 7 to 20 GHz.
- Visual examples of the different constraints to be considered in ISAC based on simulation data in Section IV,

guiding the reader through the relevant limits to be considered.

- An evaluation of selected use cases in Section V, based on the analytical model provided in this work, determining their feasibility and performance according to the foreseen features of 6G systems. This Section will highlight what are the main limiting factors constraining ISAC KPIs, defining the most pertinent questions to be addressed in ISAC cellular systems' research.
- A conclusion together with a summary of the main findings in Section VI.

II. ASSUMED MODEL

We first lay down the model used to analytically evaluate scenarios. In this document, we are considering a mono-static setup with quasi co-located uniform rectangular arrays (URAs) TX and RX of equal characteristics, with R rows and C columns, spaced Δr and Δc, respectively. This practically coincides with a full duplex sensing system, that is the likely implementation of first ISAC deployments [3]. Note that equal performance, apart from angular resolution, could be achieved with a bi-static deployment. Even though additional gains may be achieved by fusing information between multiple points at a central function, this is not considered in this work. The symbols and notations used throughout this document are defined in Table V at the end of this document.

A. Link budget with thermal noise

In order to get meaningful information, like most of the radar literature [9], we assume line of sight propagation to write the received power equation as function of the range

$$P_R(r) = \frac{P_T G_T}{4\pi r^2} \Psi \frac{1}{4\pi r^2} \frac{G_R \lambda^2}{4\pi} =$$
$$= P_T G_T G_R \cdot \Psi \cdot \frac{c_0^2}{(4\pi)^3 r^4 f_c^2} . \qquad (1)$$

Note that in [9], the transmit antenna G_T is not included (i. e., isotropic radiation is assumed), but in this document we consider it to account for the TX beamforming gains, assuming that we are perfectly focusing the target with the used transmit beam. The noise power can be written as

$$P_N = (N_0 F)(N\Delta f) , \qquad (2)$$

which allows us to define the available signal-to-noise ratio (SNR) on each single orthogonal frequency division multiplexing (OFDM) symbol

$$\gamma_S(r) = \frac{P_R(r)}{P_N} . \qquad (3)$$

The SNR is increased due to a multiplicative gain given by the number of subcarriers N and OFDM symbols M [9], resulting in an SNR of

$$\gamma(r) = \frac{P_R(r)}{P_N} NM , \qquad (4)$$

which in case of the periodogram is due to the focusing of the Fourier transform operations on the sparse representation of the radar echo.

To compute the achievable range in each scenario, an SNR of $\gamma^* = 17$ dB (after antenna gain, processing gain, etc.) is necessary to achieve robust performance, i.e., matching the Cramér-Rao lower bound (CRLB) on accuracy to attain reliable performance in terms of both false alarms and missed detections [10]. Then, for each scenario the maximum achievable range due to the noise limit can be computed as

$$r_n^* : \gamma(r_n^*) = \gamma^* = 17 \text{ dB} \approx 50 \Rightarrow \qquad (5)$$
$$r_n^* = \sqrt[4]{\frac{P_T G_T G_R \Psi c_0^2 NM}{\gamma^* (4\pi)^3 f_c^2 N_0 F N \Delta f}} =$$
$$= \sqrt[4]{\frac{P_T G_T G_R \Psi c_0^2 M}{\gamma^* (4\pi)^3 f_c^2 N_0 F \Delta f}} . \qquad (6)$$

B. Quantization noise

However, the achievable range may in practice be dictated by the strongest reflection of an object (or the direct path as self-interference). This is due to the quantization noise of a Q bit analog-to-digital-converter (ADC). One should determine the impact of the objects present in the environment, grouped in the set $\mathcal{T}$. Moreover, also self-interference between transmitter and receiver must be considered. Accordingly, the limiting factor is given by

$$\bar{t} = \max \left[\max_{t \in \mathcal{T}} \left(\frac{\Psi_t}{r_t^4} \right), \frac{\alpha 4\pi}{r_{t'}^2} \right] , \qquad (7)$$

where Ψ_t and r_t are the t-th object's radar cross section (RCS) and range. The isolation between transmitter and receiver $\alpha \leq 1$ depends on beamforming and hardware features, of transmitter and receiver, separated by $r_{t'}$ [11]. Similarly, one could trivially rewrite the self-interference part of (7), in case of co-located transmitter and receiver. Accordingly, the signal-to-quantization-noise ratio (SQNR) can be written as [12]

$$\text{SQNR}_Q = (2^Q)^2 \approx 6.02 \cdot Q \text{ dB} . \qquad (8)$$

Taking distortions due to the peak-to-average power ratio (PAPR) of the transmitted OFDM signal into account as γ_{PAPR}, which can e. g., be modeled as in [13], and assuming perfect automatic gain control, the SQNR at the receiver is

$$\gamma_Q = \frac{\text{SQNR}_Q MN}{\gamma_{\text{PAPR}}} , \qquad (9)$$

where the MN processing gain is still available after ADC quantization. Additional losses in terms of non-ideal automatic gain control can further reduce γ_Q. Note that in case of quantization with Q' bits in the fast Fourier transform (FFT) operations used for sensing, the processing gain and OFDM's PAPR should not be considered, leading to $\gamma_q(Q, Q') = \min(\gamma_Q, \text{SQNR}_{Q'})$. This is because both FFT inputs and outputs are quantized, thus leading to a quantization of the complex numbers, whose amplitude squared is already the periodogram. Accordingly, the maximum achievable range r_q^*

(guaranteeing an SNR of γ^*) due to quantization noise of a target with RCS Ψ is given by

$$\frac{\Psi}{\bar{t}\left(r_q^*\right)^4} = \frac{\gamma^*}{\gamma_q(Q,Q')} \Rightarrow$$

$$r_q^* = \sqrt[4]{\frac{\Psi\gamma_q(Q,Q')}{\bar{t}\gamma^*}} \ . \tag{10}$$

In case of being limited by an object at range $r_{\bar{t}}$ with RCS $\Psi_{\bar{t}}$, the achievable range can be written as

$$r_q^* = r_{\bar{t}} \cdot \sqrt[4]{\frac{\Psi\gamma_q(Q,Q')}{\Psi_{\bar{t}}\gamma^*}} \ . \tag{11}$$

C. Achievable accuracy

We recall that super-resolution techniques - like MU-SIC [10] – and interpolation-based algorithms – like SARA [14] - achieve the CRLB with $\gamma(r) \geq \gamma^*$. This means that the standard deviation of sensing estimates in this operating regime, i.e., $r \leq r^*$, is given by the already derived CRLB formulae in [9], that are

$$\sigma_r = \frac{c}{4\pi\Delta f}\sqrt{\frac{6}{(N^2-1)\gamma(r)}} \ , \tag{12}$$

$$\sigma_s = \frac{c}{4\pi f_c T_O}\sqrt{\frac{6}{(M^2-1)\gamma(r)}} \ , \tag{13}$$

$$\sigma_z = \frac{1}{2\pi}\sqrt{\frac{6}{(R^2-1)\gamma(r)}} \ , \tag{14}$$

$$\sigma_x = \frac{1}{2\pi}\sqrt{\frac{6}{(C^2-1)\gamma(r)}} \ . \tag{15}$$

Remark 1. *In case of clock errors between transmitter and receiver, with standard deviations of absolute clock and frequency errors – after correction algorithms – σ_t and σ_f, respectively, the range and speed standard deviations can be updated as*

$$\sigma_r' = \sqrt{\sigma_r^2 + (c\sigma_t)^2} \ , \tag{16}$$

$$\sigma_s' = \sqrt{\sigma_s^2 + \left(\frac{c}{f_c}\right)^2\sigma_f^2} \ , \tag{17}$$

where we assumed independency between clock error and thermal noise.

For angular measures, σ_x and σ_z are the corresponding normalized angular frequencys (NAFs) in horizontal (x-axis) and vertical (z-axis) direction of the receive array, respectively, described in [14]. The mapping of σ_x and σ_z to angular accuracy depends on the incident angle with respect to the system, with the highest performance at boresight. Once the incident azimuth θ and elevation ϕ are known, their NAF can be computed as

$$\eta = \frac{\Delta r}{\lambda}\sin(\phi) \ , \tag{18}$$

$$\ell = \frac{\Delta c}{\lambda}\sin(\theta)/\cos(\phi) \ . \tag{19}$$

Then, one can use inversion formulae to measure the offset corresponding to σ_z and σ_x in angles, as follows

$$\sigma_\phi = \sin^{-1}\left(\frac{\lambda}{\Delta r}(\eta \pm \sigma_z)\right) - \phi \ , \tag{20}$$

$$\sigma_\theta = \sin^{-1}\left(\frac{\lambda}{\Delta c}\cos(\phi)(\ell \pm \sigma_x)\right) - \theta \ . \tag{21}$$

D. Achievable Resolution

For the achievable resolutions, see definitions in Table V, the equations from [9], [15] can be used to get

$$\rho_r = \frac{c}{2N\Delta f} \ , \tag{22}$$

$$\rho_s = \frac{c}{2T_f f_c} \ , \tag{23}$$

$$\rho_z = \frac{1}{2R-1} \ , \tag{24}$$

$$\rho_x = \frac{1}{2C-1} \ , \tag{25}$$

where ρ_z and ρ_x are determined using the shape, i.e., vertical and horizontal, respectively, of the sum co-array of transmit and receive array [15]. We recall that the sum co-array of two URAs with $R \times C$ elements is given by a URA with $(2R-1) \times (2C-1)$ elements.

The shift to resolutions ρ_ϕ and ρ_θ in terms of the incident angles ϕ and θ is obtained in a way similar to the accuracy as

$$\rho_\phi = \sin^{-1}\left(\frac{\lambda}{\Delta r}\rho_z\right) - \phi \ , \tag{26}$$

$$\rho_\theta = \sin^{-1}\left(\frac{\lambda}{\Delta c}\cos(\phi)\rho_x\right) - \theta \ . \tag{27}$$

These angular resolutions can be further translated into a required spacing in meters between two objects at distance r from the base station. For simplicity, we consider the vertical direction resolution ρ_v (depending only on the elevation ϕ) and the horizontal direction resolution ρ_h (depending on both azimuth θ and elevation ϕ) separately. They are given as

$$\rho_v = r \cdot \sin\left(\rho_\phi\right) \ , \tag{28}$$

$$\rho_h = r \cdot \sin\left(\rho_\theta\right) \ . \tag{29}$$

This allows us also to write the maximum range achievable due to the angular resolution r_a^*, if we require a vertical/horizontal resolution of ρ_v^*, ρ_h^*, respectively, as

$$r_v^* = \frac{\rho_v^*}{\sin(\rho_\phi)} \ , \tag{30}$$

$$r_h^* = \frac{\rho_h^*}{\sin(\rho_\theta)} \ . \tag{31}$$

However, targets need to be separated just in one domain, thus the best performing resolution direction dominates. Therefore, one should consider the maximum between r_h^* and r_v^*, and only if range and speed resolutions do not allow separating targets reliably.

E. Unambiguous Ranges

The achievable performance may further be limited by the unambiguous ranges (i. e., maximum values without ambiguities due to aliasing). For range and speed, the maximum unambiguous values are

$$r_u^* = \frac{c_0}{2\Delta f} , \qquad (32)$$

$$s_u = \frac{c_0}{2 f_c T_0} . \qquad (33)$$

F. Achievable sensing range

All the considerations in the previous subsections allow us to finally write the achievable sensing range r^* as the most stringent constraint imposed by thermal noise, quantization noise, angular resolution, and unambiguous range. In particular, we have

$$r^* = \min \left(r_n^*, r_q^*, \max(r_v^*, r_h^*), r_u^* \right) , \qquad (34)$$

if range and speed resolution do not allow to reliably separate targets in the use case of interest. Otherwise, e. g., in case of moving target detection with a high enough speed resolution to separate the target from static clutter, one could neglect angular resolution dependencies as follows

$$r^* = \min \left(r_n^*, r_q^*, r_u^* \right) . \qquad (35)$$

Remark 2. *Equations* (34) *and* (35) *assume line of sight (LoS) between object and radar, which may not be the case in practice. LoS probability is, however, hard to model, and therefore left out of this discussion.*

III. SYSTEM PARAMETERS

In this Section, we illustrate the likely parameters of the next generation of cellular networks. The proposed values for FR1, FR2, and FR3 are listed in Table I, and they will be used in Section V to evaluate use cases' feasibility. In every frequency range, we assume antenna radiator elements with gain $G_E = 2 = 3$ dBi. The resulting array gain accounts also for the number of elements, as follows

$$G_T = RC G_E . \qquad (36)$$

For FR1, the values are based on currently available white papers by the industry [16], [17]. Note that the 24×8 elements are given by assuming 6 radiators vertically stacked per antenna port, resulting in an equivalent 4×8 digital system. The radio transmission features are taken from Table 5.3.2-1 of TS 38.101-1 [4], dictating the number of subcarriers N given the specific carrier aggregation parameters. In FR1, we assume 2×100 MHz carrier aggregation, corresponding to $N = 6552$ and transmit power for outdoor scenarios $P_{T,O} = 49$ dBm.

For FR2, we based our assumptions on a running mmWave system at 28 GHz, showcased at 2023 Mobile World Congress [3]. We doubled the array size to 32×32 and the total bandwidth to 8×200 MHz, accounting for the evolution of hardware in the next years.

For FR3, we assume 1024 elements, as most of the recent literature [16], doubling the bandwidth of FR1 systems to 4×100 MHz, using the same transmit power $P_{T,O} = 49$ dBm as in FR1 for outdoor scenarios.

Considering indoor use cases, the European regulations [18] on electromagnetic field exposure fix the power density limit to $S_0 = 10$ W/m^2 in the frequencies of interest. Accordingly, assuming a minimum distance of $d' = 1$ m between transmitter and humans, the transmit power limit for indoor scenarios is

$$P_{T,I} = \frac{S_0 4\pi d'^2}{G_T T^* P^*} , \qquad (37)$$

where T^* and P^* are the time division duplex (TDD) duty-cycle and the power reduction factor applicable due to beam steering and time averaging, respectively. In this work, we consider $T^* = 80\%$, while $P^* = 0.25$ is assumed from [19].

To determine the number of OFDM symbols M, we consider the positioning reference signal (PRS) for sensing in the downlink (DL), whose configuration options are defined in [20]. Configuring the number of OFDM symbols that are allocated for PRS per slot L_{PRS} and the comb size $K_{\mathrm{comb}}^{\mathrm{PRS}}$ such that the number of transmitted PRS symbols per slot is maximized leads to $M_{\mathrm{slot}}^{\mathrm{PRS}} = 6$ (option $\{L_{\mathrm{PRS}} = 12, K_{\mathrm{comb}}^{\mathrm{PRS}} = 2\}$ [20]). Then, choosing offsets and periodicity properly, PRS can be configured for transmission in every slot. The final values for the number of OFDM symbols per radio frame M are obtained by accounting for a $1 - T^* = 20\%$ TDD overhead.

TABLE I. CONSIDERED SYSTEM PARAMETERIZATIONS

Parameter	FR1	FR2	FR3
f_c	3.5 GHz	28 GHz	7 GHz
B	200 MHz	1600 MHz	400 MHz
Δf	30 kHz	120 kHz	60 kHz
T_0	35.67 µs	8.92 µs	17.84 µs
N	6552	12672	6480
M	96	384	192
F	8 dB	8 dB	8 dB
G_T	25.8 dB	33 dB	33 dB
G_E	3 dBi	3 dBi	3 dBi
R, C	24, 8	32, 32	32, 32
$\Delta r, \Delta c$	0.7λ, 0.5λ	0.5λ, 0.5λ	0.5λ, 0.5λ
$P_{T,O}$	49 dBm	36 dBm	49 dBm
$P_{T,I}$	32.2 dBm	25 dBm	25 dBm
Q	12	12	12

IV. VISUAL EXAMPLES OF ISAC LIMITS

Before discussing selected use cases in Section V, we provide visualizations of some of the discussed ISAC constraints introduced in Section II. Those examples are intended to give the reader a better understanding in order to make the following use cases discussion easier to follow.

In Fig. 1, four different range-angle periodograms are visualized. The two periodograms on the left illustrate the effect of resolution. The leftmost image is obtained with the FR1 system parameterization from Table I, with two close targets in both range and angle. One can observe that the poor resolution due to the limited antenna aperture and available bandwidth
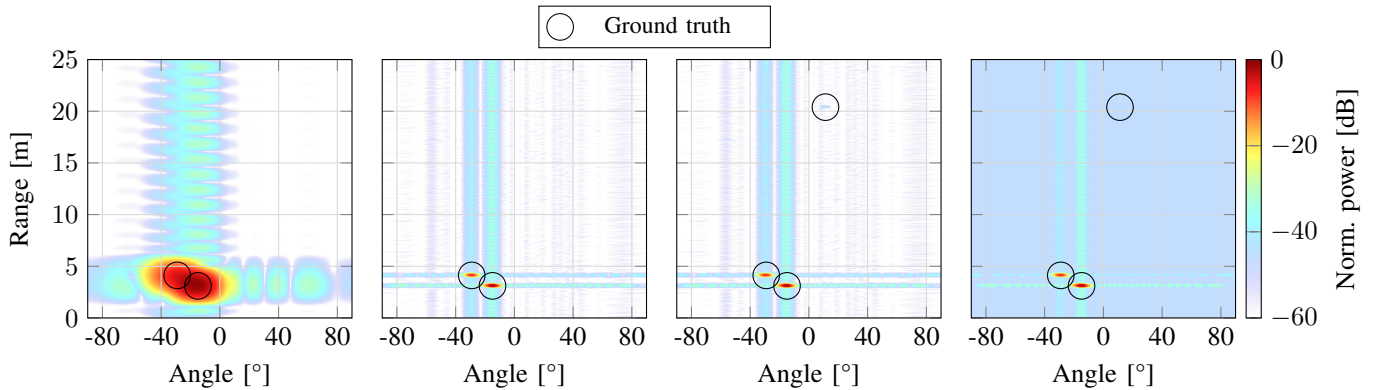
Fig. 1: Periodograms of exemplary scene including thermal noise and configuration according to Tab. I: (1) one observable target for FR1, (2) higher resolution in FR2 enables separation of two close targets, (3) third target further away distinguishable, (4) third target covered by quantization noise after $Q' = 8$ bit quantization.

does not allow discriminating the two close targets (marked by black circles), resulting in the detection of only a single one. In the periodogram right beside the first, on the other hand, both targets are resolvable due to the FR2 system providing higher bandwidth and array horizontal aperture, resulting in sufficient range and angle (i. e., spatial) resolution capabilities.

We continue by discussing the impact of quantization noise. The second periodogram from the right displays the case where no quantization noise is considered, enabling the detection of an additional target that is further away at a range of ≈ 20 m. In the rightmost figure, however, a further quantization in the FFT operations is assumed with $Q' = 8$ bits. This causes the farther target to "drown" in quantization noise, blinding it out from the resulting periodogram and rendering its detection infeasible.

These simplified examples serve to show that resolution capabilities and quantization might play a critical role in determining the achievable performance of ISAC systems. Therefore, they should be taken into account for the following use cases investigation, together with the link budget considerations of Subsection II-A.

V. USE CASES INVESTIGATION

In this section, we investigate three families of emerging ISAC use cases: 1) Indoor Factory Safety (V-A), 2) Roadway Monitoring (V-B), and 3) Outside Drone Detection (V-C). First, assuming LoS and using the foundations established in the previous sections, Table II displays a list of achievable sensing KPIs in FR1 and FR2, at the range at which the minimum required sensing SNR of $\gamma^* = 17$ dB is attained. For each use case, we will focus on the most relevant KPIs and from those we try to draw conclusions on the scenario's feasibility.

Furthermore, Table III lists the maximum achievable sensing ranges due to the noise limit (Eq. (12)) for objects that are of interest for the investigated use cases, along with their assumed RCS values from literature [21], [22]. As one can deduce from

TABLE II. SENSING PERFORMANCE PARAMETERS WITH SNR = 17 dB) AND LoS CONDITION

Parameter	FR1	FR2	FR3
σ_r [m]	0.042	0.005	0.021
σ_v [m/s]	0.689	0.086	0.345
σ_ϕ (boresight) [°]	3.71	3.9	3.9
σ_θ (boresight) [°]	15.74	3.9	3.9
ρ_r [m]	0.76	0.1	0.39
ρ_s [m/s]	4.29	0.54	2.14
ρ_ϕ (boresight) [°]	1.74	1.82	1.82
ρ_θ (boresight) [°]	7.66	1.82	1.82
ρ_v (boresight) [m]	0.03r	0.032r	0.032r
ρ_h (boresight) [m]	0.133r	0.032r	0.032r
r_u^* [m]	5000	1250	2500
s_u [m/s]	600.7	300.3	600.6

Table III, sensing performance is – for the systems we assumed in Section III – not limited by thermal noise. In addition to resorting to literature, an alternative way to estimate the RCS is suggested by [9]. One could take measurements with a given setup, estimate the periodogram's peak value $\hat{p}$ and range $\hat{r}$, corresponding to the target, and invert (1) to get

$$\hat{\Psi} = \hat{p} \frac{(4\pi)^3 \hat{r}^4 f_c^2}{P_T N M G_T G_R c_0^2} \ . \tag{38}$$

Remark 3. *The values in Table III suggest that typical objects of interest can be sensed kilometers away. However, those are the maximum achievable ranges due to the noise limit, determined with (6). As discussed in Section II, quantization noise, resolution limitations, and unambiguous range must be considered as well. In what follows, we show that the last mentioned constraints are the dominating factors in practice in all considered use cases. Therefore, one could deduce that sensing performance is - for the systems we assumed in Section III - typically not limited by thermal noise.*

Remark 4. *The precise extent of the quantization impact is highly dependent on the scenario. Since the presence of*

TABLE III. MAX. RANGE FOR DIFFERENT OBJECTS DUE TO THERMAL NOISE LIMIT (SNR = $\gamma^* = 17$ dB)

Outdoor ($P_{T,O}$)				
Object	Ψ **[m^2]**	r_n^* **(FR1) [km]**	r_n^* **(FR2) [km]**	r_n^* **(FR3) [km]**
Drone	0.1	7.65	3.01	12.23
Human	1	13.39	5.27	21.44
Car	100	41.18	16.51	65.99
Indoor ($P_{T,I}$)				
Drone	0.1	2.99	1.63	3.19
Human	1	5.23	2.85	5.58
AGV	2	6.19	3.37	6.61

strong close reflectors is hard to model, we will for the most part disregard the quantization limitation in the following use case analysis. However, it must be kept in mind when evaluating/planning specific sensing deployments.

A. Indoor Factory Safety

As the first use case, an indoor factory scenario is considered. Such a typically cluttered environment with multiple and possibly closely spaced reflectors requires high spatial resolution capabilities, achievable via a high total bandwidth B (for range resolution ρ_r) and a large number of antennas (for angular resolution ρ_θ and ρ_ϕ). Moreover, a good velocity resolution ρ_s provides another degree of freedom, that may be leveraged to discriminate moving targets of interest from reflections caused by static background clutter. We therefore regard systems in FR3 and especially FR2 as suitable for this scenario, since the larger path loss in the millimeter-wave range can be tolerated as only short distances, i.e., $r \approx$ 10-20 m, must be supported inside a factory. On the other hand, the achievable resolutions $\rho_r = 0.76$ m and $\rho_h = 0.133r \approx$ 1.3-2.7 m in FR1 will presumably not be sufficient to cover most interesting applications, as it becomes harder to separate objects of interest from the background clutter.

Sufficient distances will likely be possible for sensing objects of interest, such as humans or automated guided vehicles (AGVs), even in case the maximum achievable range is considerably reduced by the presence of strong reflecting objects due to quantization. Therefore, in cluttered factory environments, we think that resolution will be the limiting factor. For instance, if one aims at detecting objects at similar range with a horizontal separation of $\rho_h^* = 0.5$ m, one could achieve this performance up to a range of $r^* = 15.25$ m from the sensing point in FR2 and FR3, while only $r^* = 3.8$ m would be possible for FR1. In FR2, the high range resolution of $\rho_r = 0.1$ m may additionally be leveraged, which is why we consider FR2 most suitable for indoor factories. Nonetheless, due to blockers and non-line of sight (NLOS) conditions, multiple transmission and reception points (TRPs) will likely still be required to offer reliable sensing services over a wide area in a factory.

Remark 5. *Since we always assume an equal SNR $\gamma^* = 17$ dB – and not an equal sensing range – for determining the*

sensing KPIs in Table II, better accuracies can obviously be achieved for sensing a stronger reflector (AGV in this case) at the same distance as a weaker reflector (human body), due to the larger RCS and thus resulting higher SNR.

B. Roadway Monitoring

The second family of use cases in this document is concerned with roadway monitoring. In that context, applications such as traffic count, ghost driver detection (i.e., detecting a vehicle moving in the wrong direction of traffic on a highway), or pedestrian/animal detection are conceivable and will be addressed in the following.

To cover as much of the street as possible, it may initially appear favorable to operate in FR1. Most use cases, however, will not have to monitor the entire roadway (especially in case of long highways), but only certain points of interest (e.g., traffic count) or at regular intervals (e.g., ghost driver detection). Moreover, such applications will likely be limited by the resolution rather than by the range, so in the following we mainly consider FR2 and FR3.

1) Traffic Count: In view of this use case, the spatial resolution capabilities are of interest, since for traffic count it is required to discriminate two vehicles driving in different lanes. As introduced in Section II, horizontal and vertical direction resolution are considered separately. We further assume that the base station "observing" the roadway is placed at a height of a few meters, such that vehicles driving within a lane can be treated almost as radial movements, i.e., towards the base station. To discriminate vehicles in different lanes, the horizontal direction resolution of $\rho_h = 0.032r$ from Table II can then be leveraged. This allows distinguishing two vehicles on separate lanes up to a distance of ca. $r^* = 78$ m, where a spacing of at least $\rho_h^* = 2.5$ m between them is assumed. While this value represents the horizontal resolution at boresight, which is not always attainable in practice, the high range and speed resolutions can further help. As in the factory scenario, one can make use of the range resolution of ca. 0.1 m in FR2, which even allows discriminating different vehicles in the same lane. Moreover, for counting traffic it is enough to merely detect the presence of multiple vehicles rather than being able to perfectly resolve them.

Remark 6. *The ability to resolve different objects also depends on the objects' dimensions, as e.g., a long truck might cause several reflections. Those influences are again hard to model, however, and are therefore omitted from the discussions in this work.*

2) Ghost Driver Detection: Ghost Driver Detection is in many regards similar to the traffic count use case. The requirements are now slightly less stringent, since a ghost driver moves in the opposite direction than cars on the same side of the road such that the Doppler (i.e., speed/velocity) domain can be used to discriminate them. Nonetheless, a ghost driver must still be distinguishable from other cars driving in the same direction at similar velocities, but using the correct lane. Accordingly, horizontal resolution is necessary also in this

TABLE IV. SUMMARY OF INVESTIGATED USE CASES

Use Case	Frequency Range(s)	Limiting Factor(s)	Max. Sensing Range r^*
Indoor Factory Safety	FR2	NLOS conditions, System resolution	15 m for $\rho_h^* = 0.5$ m, probably lower due to NLOS
Traffic Count	FR2, FR3	Horizontal resolution	$50 - 100$ m
Ghost Driver Detection	FR2, FR3	Horizontal resolution	$100 - 200$ m
Pedestrian Crossing Detection	FR2, FR3	Horizontal resolution	$20 - 40$ m
Outside Drone Detection	FR1, FR3, FR2 (less preferred)	Unambiguous range, NLOS conditions	5000 m (FR1), 2500 m (FR3), 1250 m (FR2)

case. Two cars on opposite lanes could be distinguished up to a distance of ca. $r^* = 156$ m, where a spacing of at least $\rho_h^* = 5$ m between them is now assumed due to the higher spacing of lanes in opposite directions. It should be noted that tracking techniques can further help discriminating different vehicles from the history of collected measures, likely further extending the achievable range in practice.

3) Pedestrian Crossing Detection: As a consequence of the previously discussed resolution limitations, it appears unfeasible to reliably monitor big segments of a roadway for people (or animal) crossing detection use cases. However, sensing systems may still be deployed to detect humans in particularly dangerous areas, e. g., at railway crossings. The spatial resolution capabilities will likely again be the limiting factor, as pedestrians on a crossing should be distinguishable from people moving along "safe paths" next to the road or railway. Hence, FR2 and FR3 are again preferable due to offering the best spatial resolution capabilities. Assuming a required $\rho_h^* = 1$ m leads to an achievable range of $r^* = 31.25$ m.

C. Outside Drone Detection

As the last use case, outside drone detection is discussed. Since drone detection may be of interest in different settings/environments (e. g., urban macro, airport, etc.), all three frequency ranges can be considered for this application. Operating in FR1 enables a higher achievable sensing range and allows to leverage deployments designed mainly for communications coverage, but also offers worse capabilities w. r. t. accuracy and resolution. This trade-off in favor of the sensing range, however, appears acceptable, as typically drones fly in open space, and detection is more important than precisely localizing and counting them, for which resolution plays a critical role. According to (35) and system parameters, the system will be limited mainly by unambiguous range, resulting in $r^* = 5000$ m for FR1, $r^* = 1250$ m in FR2, and $r^* = 2500$ m for FR3. Therefore, operating in FR1 or FR3 is generally advocated for the use case of outside drone detection. FR2 should also not be precluded, especially if the scenario requires higher resolution capabilities and/or the maximum required sensing range is low.

Finally, Table IV summarizes this investigation by providing an overview of the suggested frequency range(s), limiting factor(s), and maximum achievable sensing range for each use case.

VI. CONCLUSION

In this paper, we have derived an analytical model for ISAC performance assessment taking practical limitations into account. Based on our framework and system paremeterizations that can be expected for the main 6G frequency ranges, we evaluated emerging ISAC use cases w. r. t. sensing KPIs, and drew first preliminary conclusions about their feasibility. Further, visual examples of the most meaningful practical limitations of ISAC systems have been provided by means of simulations.

We concluded that the main limiting factor for sensing in 6G ISAC systems will be LoS coverage and spatial resolution. While the first can be addressed with densification accompanied by considerable costs, the second can be addressed by further increasing array sizes of current ISAC systems, especially in the horizontal direction.

While this work only represents a first step towards a complete analytical characterization of ISAC systems, the authors believe that it can help in better understanding their practical limitations together with their implications on possible use cases.

REFERENCES

[1] H. Viswanathan and P. E. Mogensen, "Communications in the 6G era," *IEEE Access*, vol. 8, pp. 57 063–57 074, 2020.

[2] F. Liu, Y. Cui, C. Masouros, J. Xu, T. X. Han, Y. C. Eldar, and S. Buzzi, "Integrated sensing and communications: Towards dual-functional wireless networks for 6G and beyond," *IEEE journal on selected areas in communications*, 2022.

[3] T. Wild, A. Grudnitsky, S. Mandelli, M. Henninger, J. Guan, and F. Schaich, "6G Integrated Sensing and Communication: From Vision to Realization," *arXiv 2305.01978*, 2023. [Online]. Available: https://arxiv.org/abs/2305.01978

[4] 3GPP, "User Equipment (UE) radio transmission and reception; Part 1: Range 1 Standalone," Technical Specification Group RAN, Technical Specification 38.301-1, 2023, Version 17.8.0 (Rel. 17).

TABLE V. NOTATION USED IN THIS DOCUMENT

P_R	Received power [W]
P_T	Transmitted power [W]
$P_{T,O}$	Transmitted power in outdoor scenarios [W]
$P_{T,I}$	Transmitted power in indoor scenarios [W]
P_N	Noise power [W]
N_0	Thermal noise spectral density = -174 [dBm/Hz]
F	Noise figure
γ_S	SNR on each OFDM sample
γ	SNR after processing gains
γ^*	Min. required SNR
γ_q	Max. SQNR at the receiver
G_T	Total transmit antenna array gain
G_R	Total receive antenna array gain
G_E	Single array element gain
S_0	Maximum transmit power density [10 W/m^2]
T^*	TDD duty-cycle
P^*	Electromagnetic field limit power reduction factor due to beam steering and time averaging
r	Range [m]
r^*	Max. supported range [m]
α	Isolation between transmitter and receiver
Ψ	Radar cross section [m^2]
λ	Wavelength [m]
c_0	Speed of light in vacuum [m/s]
f_c	Central frequency [Hz]
Δf	Subcarrier spacing [Hz]
N	Number of subcarriers
T_0	OFDM symbol duration incl. cyclic prefix [s]
T_f	Frame duration [s]
M	Number of OFDM symbols
R, C	Number of antenna rows, columns
$\Delta r, \Delta c$	Antenna spacing between rows, columns [m]
σ_r	Range standard deviation [m]
σ_s	Speed standard deviation [m/s]
σ_z	Standard deviation w.r.t. vertical array direction (z-axis) [NAF]
σ_ϕ	Elevation standard deviation [°]
σ_x	Standard deviation w.r.t. horizontal array direction (x-axis) [NAF]
σ_θ	Azimuth standard deviation [°]
σ_t	Clock timing error standard deviation [s]
σ_f	Clock frequency error standard deviation [Hz]
ρ_r	Range resolution [m]
ρ_s	Speed resolution [m/s]
ρ_z	Resolution w.r.t. vertical array direction (z-axis) [NAF]
ρ_ϕ	Elevation resolution [°]
ρ_v	Vertical direction resolution [m]
ρ_x	Resolution w.r.t. horizonal array direction (x-axis) [NAF]
ρ_θ	Azimuth resolution [°]
ρ_h	Horizontal direction resolution [m]
r_u	Unambiguous range [m]
s_u	Unambiguous speed [m/s]

[5] ——, "User Equipment (UE) radio transmission and reception; Part 2: Range 2 Standalone," Technical Specification Group RAN, Technical Specification 38.301-2, 2023, Version 17.8.0 (Rel. 17).

[6] M. Henninger, T. E. Abrudan, S. Mandelli, M. Arnold, S. Saur, V.-M. Kolmonen, S. Klein, T. Schlitter, and S. Ten Brink, "Probabilistic 5G Indoor Positioning Proof of Concept with Outlier Rejection," in *2022 Joint European Conference on Networks and Communications & 6G Summit (EuCNC/6G Summit)*. IEEE, 2022, pp. 249–254.

[7] A. Liu, Z. Huang, M. Li, Y. Wan, W. Li, T. X. Han, C. Liu, R. Du, D. K. P. Tan, J. Lu *et al.*, "A survey on fundamental limits of integrated sensing and communication," *IEEE Communications Surveys & Tutorials*, vol. 24, no. 2, pp. 994–1034, 2022.

[8] "HEXA-X-II project," https://hexa-x-ii.eu/.

[9] K. M. Braun, "OFDM radar algorithms in mobile communication networks," Ph.D. dissertation, Karlsruhe, Karlsruher Institut für Technologie (KIT), Diss., 2014, 2014.

[10] B. A. Johnson, Y. I. Abramovich, and X. Mestre, "MUSIC, G-MUSIC, and Maximum-Likelihood Performance Breakdown," *IEEE Transactions on Signal Processing*, vol. 56, no. 8, pp. 3944–3958, 2008.

[11] C. D. Nwankwo, L. Zhang, A. Quddus, M. A. Imran, and R. Tafazolli, "A survey of self-interference management techniques for single frequency full duplex systems," *IEEE Access*, vol. 6, pp. 30 242–30 268, 2017.

[12] W. R. Bennett, "Spectra of quantized signals," *The Bell System Technical Journal*, vol. 27, no. 3, pp. 446–472, 1948.

[13] A. Behravan and T. Eriksson, "PAPR and other measures for OFDM systems with nonlinearity," in *The 5th International Symposium on Wireless Personal Multimedia Communications*, vol. 1. IEEE, 2002, pp. 149–153.

[14] S. Mandelli, M. Henninger, and J. Du, "Sampling and Reconstructing Angular Domains with Uniform Arrays," *IEEE Transactions on Wireless Communications*, 2022.

[15] R. T. Hoctor and S. A. Kassam, "The unifying role of the coarray in aperture synthesis for coherent and incoherent imaging," *Proceedings of the IEEE*, vol. 78, no. 4, pp. 735–752, Apr. 1990.

[16] S. Wesemann, J. Du, and H. Viswanathan, "Energy Efficient Design of Extreme Massive MIMO," *arXiv preprint arXiv:2301.01119*, 2023.

[17] H. Holma, H. Viswanathan, and P. Mogensen, "Extreme massive MIMO for macro cell capacity boost in 5G-advanced and 6G," in *White paper*. Nokia Bell Labs, 2021.

[18] Council of Recommendation, "Limitation of exposure of the general public to electromagnetic fields (0 Hz to 300 GHz)," *Official Journal of the European Communities*, vol. 199, 1999.

[19] P. Baracca, A. Weber, T. Wild, and C. Grangeat, "A statistical approach for RF exposure compliance boundary assessment in massive MIMO systems," in *WSA 2018; 22nd International ITG Workshop on Smart Antennas*. VDE, 2018, pp. 1–6.

[20] 3GPP, "Physical channels and modulation," Technical Specification Group RAN, Technical Specification 38.211, 2023, Version 17.4.0 (Rel. 17).

[21] M. I. Skolnik, "Introduction to radar systems," *New York*, 1980.

[22] Á. D. de Quevedo, F. I. Urzaiz, J. G. Menoyo, and A. A. López, "Drone detection and radar-cross-section measurements by RAD-DAR," *IET Radar, Sonar & Navigation*, vol. 13, no. 9, pp. 1437–1447, 2019.